



Cite this: *Phys. Chem. Chem. Phys.*,
2025, 27, 12190

Enhancing electrocatalytic CO₂ reduction via engineering substrate–cluster interaction[†]

Qian Sun,^a Huiru Yang,^{*,a} Chunmei Zhang ^{*,a,c} and Aijun Du ^b

Cu clusters exhibit exceptional performance in the electrocatalytic carbon dioxide reduction reaction (CO₂RR) due to their tunable size. Using first-principles calculations, we systematically investigate the CO₂RR on small Cu_n clusters ($n = 3, 8, 13$) anchored on a T'-WTe₂ substrate, denoted as Cu_n@T'-WTe₂. Given that the hydrogen evolution reaction (HER) often competes with the CO₂RR, we further investigated the competition between the CO₂RR and HER. Our results show that Cu_n@T'-WTe₂ outperforms pure Cu_n clusters as catalysts, with enhanced CO₂RR activity. The CO₂RR performance of Cu_n@T'-WTe₂ enhances with increasing cluster size, and surpasses the HER activity in Cu₁₃@T'-WTe₂. This enhancement stems from the substrate–cluster interactions, where the buckled “non-uniform surface” of T'-WTe₂ deforms the larger Cu₁₃ cluster, optimizing the CO₂RR efficiency. We propose a potential strategy for WTe₂-supported Cu clusters to boost CO₂RR while suppressing HER by leveraging substrate-supported Cu clusters.

Received 23rd April 2025,
Accepted 15th May 2025

DOI: 10.1039/d5cp01541c

rsc.li/pccp

1. Introduction

The accumulation of greenhouse gases, particularly carbon dioxide (CO₂), drives global warming and poses significant environmental and energy challenges.^{1,2} To address rising energy demands and mitigate CO₂ emissions, researchers have explored various strategies to convert CO₂ into valuable chemicals and feedstocks,³ including chemical reforming,^{4,5} bioconversion,⁶ photocatalysis,^{7,8} and electrocatalysis.^{9,10} Among them, the electrochemical CO₂ reduction reaction (CO₂RR) stands out as a promising approach, transforming CO₂ into valuable products^{8,10–12} like methane (CH₄),^{6,13} formic acid (HCOOH),¹⁴ and methanol (CH₃OH).^{15,16} However, the CO₂RR faces challenges such as low efficiency and poor product selectivity^{4,9,17} exacerbated by the competing hydrogen evolution reaction (HER), which significantly reduces the performance of the CO₂RR.¹⁸

To overcome these limitations, significant efforts have focused on designing efficient electrocatalysts that activate inert CO₂ molecules while suppressing the competitive HER. Various systems, including metals,^{19,20} metal oxides,^{21,22} clusters,²³ carbon-based materials,^{24,25} and metal-organic frameworks,^{26,27} have been explored. Among them, clusters, in particular Cu clusters, demonstrate excellent CO₂RR catalytic

performance.^{28,29} When supported on substrates, the synergistic interaction between the substrate and cluster significantly influences the CO₂RR efficiency.³⁰ Thus, optimizing the substrate–cluster pairing is critical to maximizing the CO₂RR activity and minimizing HER interference.

In this study, we employ first-principles calculations to examine the CO₂RR performance of Cu_n clusters ($n = 3, 8, 13$) anchored on a T'-WTe₂ substrate denoted as Cu_n@WTe₂.^{31–33} Compared to unsupported Cu_n (Cu₃, Cu₈, and Cu₁₃),^{28,34–36} our findings reveal that the T'-WTe₂ substrate reduces the absolute limiting potential for the CO₂RR process ($|U_L|$),³⁷ while inhibiting the competitive HER. This improvement is attributed to the strong distortion of larger Cu₁₃ clusters by the buckled T'-WTe₂ surface, facilitating rapid charge transfer between the cluster and substrate. Our work provides an effective approach for enhancing CO₂RR efficiency *via* engineering substrate–cluster interactions.

2. Computational methods

Spin-polarized density functional theory (DFT) calculations were carried out using the Vienna ab initio simulation package (VASP).^{38,39} The projector-augmented-wave (PAW) method was employed to treat the core wave functions.⁴⁰ The generalized gradient approximation (GGA) in the Perdew–Burke–Ernzerhof (PBE) form is adopted.^{41,42} Long-range van der Waals (vdW) interaction was corrected using the DFT-D3 scheme,⁴³ and a vacuum space exceeding 20 Å was used to minimize periodic interactions. The 3 × 3 × 1 Monkhorst–Pack *k*-points in the Brillouin zone are sampled for structural optimizations, and

^a School of Physics, Northwest University, Xi'an 710127, China.

E-mail: y1573349346@163.com, chunmeizhang@nwu.edu.cn

^b School of Chemistry and Physics and QUT Center for Materials Science, Queensland University of Technology (QUT), Brisbane, QLD 4000, Australia

^c Shaanxi Key Laboratory for Theoretical Physics Frontiers, Xi'an 710127, China

† Electronic supplementary information (ESI) available. See DOI: <https://doi.org/10.1039/d5cp01541c>

dense $6 \times 6 \times 1$ k -meshes are set for the density of states (DOS) calculations for T'-WTe₂. 15 Å \times 15 Å \times 15 Å cubic cells are used to optimize the isolated Cu₃, Cu₈ and Cu₁₃ clusters before loading on the WTe₂ surfaces. The cutoff energy for the plane wave basis is 400 eV in all the calculations, and the energy and force convergence criterion are respectively set to 10⁻⁵ eV and 10⁻² eV Å⁻¹. We used VASPsol for the implicit solvation calculations.⁴⁴ Water is considered as the continuum solvent throughout, with a bulk static dielectric constant ϵ_s of 80.⁴⁵ In addition, canonical *ab initio* molecular dynamics simulations (AIMDs) with a Nosé thermostat and integrating time with the Verlet algorithm at a time step of 1 fs are employed to investigate the thermodynamic stability of the catalyst.⁴⁶

The isolated CO₂ molecule is simulated in a large cubic cell of 15 Å in length. The adsorption energies are calculated according to the equation $E_{\text{ads}} = E_{\text{adsorbed-system}} - E_{\text{molecule}} - E_{\text{catalyst}}$, where $E_{\text{adsorbed-system}}$, E_{molecule} , and E_{catalyst} are the total energies of the catalyst with CO₂^{*}, the isolates CO₂ molecule and Cu_n@WTe₂ ($n = 3, 8, 13$), respectively. The Bader charge, charge density difference, and DOS are calculated to clarify the interactions between the adsorbed molecule and the catalyst surface. To calculate the free energy profiles of the electrocatalytic CO₂RR, the computational electrode model (CHE) is employed.⁴⁷ The free energy change (ΔG) at each elementary step of the CO₂RR process is calculated using the equation $\Delta G = \Delta E + \Delta ZPE - T\Delta S$, where ΔE is the total energy change

calculated by DFT, ΔZPE is the zero-point energy correction through frequency analysis, and T and ΔS are the reaction temperature ($T = 298.15$ K) and the entropy value change, respectively. The limiting potential (U_L) is defined as the maximum free energy change using the relation $U_L = -\Delta G_{\text{PDS}}/e$, where ΔG_{PDS} is the maximum free energy increase in a potential determining step (PDS). In addition, we utilized the post-processing functionalities provided by qvasp and VASPKIT to analyze the computational results.⁴⁸

For isolated Cu_n clusters, our calculations show finite magnetic moments (1 μ_B for Cu₃, 0 μ_B for Cu₈, and 5 μ_B for Cu₁₃), in line with previous data.^{49,50} However, when supported on the T'-WTe₂ substrate, the whole system becomes nonmagnetic. The charge transfer between the clusters and substrate fully quenches the magnetism.

3. Results and discussion

3.1. Structural models of Cu_n ($n = 3, 8, 13$) clusters, CO₂ adsorption on Cu_n and CO₂RR on Cu_n

The most stable structures of Cu₃, Cu₈, and Cu₁₃ are an equilateral triangle geometry with C_{2v} symmetry,³⁴ a tetragonal crystal with D_{2d} symmetry,³⁶ and an icosahedron geometry with I_h symmetry (see Fig. 1a–c),^{35,51} respectively. The calculated Cu–Cu bond lengths ($L_{\text{Cu–Cu}}$) are 2.34 Å for Cu₃, 2.30–2.50 Å for Cu₈, and 2.53 Å for Cu₁₃, which agree well with previously reported values.^{36,49,50,52}

We first examine CO₂ adsorption on Cu_n ($n = 3, 8, 13$) clusters. The most stable adsorption configurations are depicted in Fig. 1d–f, revealing a bent CO₂ geometry on all Cu_n clusters, which indicates effective activation of the CO₂ molecule. For the CO₂RR, CH₄ is the sole product across all cluster sizes; however, the potential-determining step (PDS) varies with cluster size, and the overpotential increases as the cluster size grows (see Table 1). The calculated free energy profile and the corresponding reaction intermediates along the most favorable CO₂RR pathway are provided in the ESI† (see Fig. S1 and S2). Additionally, we further investigate the HER on the Cu_n cluster (Fig. 1g–i). A comparison of U_L between CO₂RR and HER, presented in Table 1, shows that the HER suppresses the CO₂RR on all pure Cu_n clusters (see Fig. S13, ESI†).

3.2. Geometric structures of T'-WTe₂

To investigate whether substrate selection can enhance CO₂RR performance, we build on our prior findings identifying T'-WTe₂ as an effective substrate that could interact with clusters

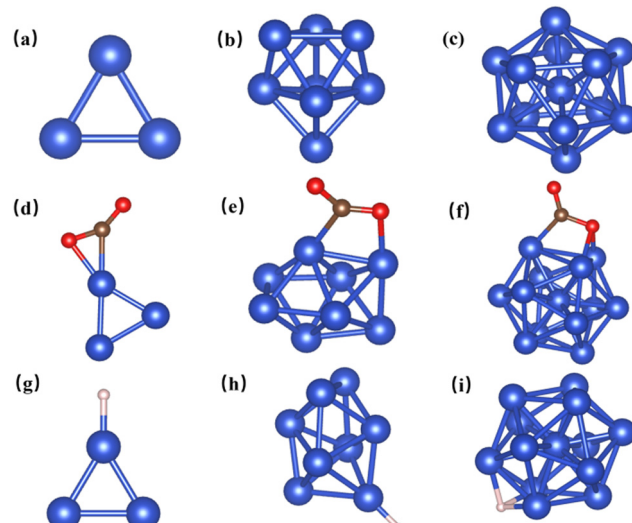


Fig. 1 (a)–(c) Structures of the pristine Cu₃, Cu₈ and Cu₁₃ clusters. (d)–(f) The most stable adsorption configurations for CO₂ on Cu₃, Cu₈, and Cu₁₃ clusters. (g)–(i) The optimized configurations for H adsorption on Cu₃, Cu₈, and Cu₁₃.

Table 1 Calculated PDS and U_L and the final product of the CO₂RR with Cu_n ($n = 3, 8, 13$) catalysts in contrast to the HER

Configurations	CO ₂ RR			HER U_L (V)
	PDS	U_L (V)	Product	
Cu ₃	$^*\text{CO} + \text{e}^- + \text{H}^+ \rightarrow ^*\text{CHO}$	0.64	CH ₄	-0.51
Cu ₈	$^*\text{OCHOH} + \text{e}^- + \text{H}^+ \rightarrow ^*\text{CHO} + \text{H}_2\text{O}$	0.85	CH ₄	0.73
Cu ₁₃	$^*\text{CO} + \text{e}^- + \text{H}^+ \rightarrow ^*\text{CHO}$	0.89	CH ₄	-0.14

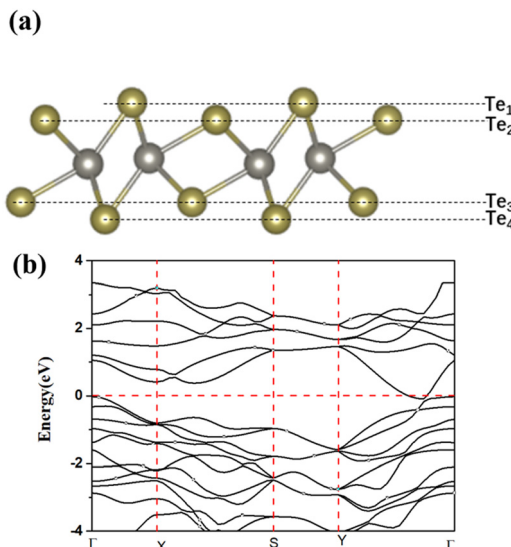


Fig. 2 (a) Schematic of the 3×2 supercell of T'-WTe₂. W and Te atoms are denoted by grey and orange spheres, respectively. (b) Band structure for the T'-WTe₂ monolayer.

sufficiently.^{30,53} Consequently, we selected T'-WTe₂ as the substrate for loading clusters to further evaluate its CO₂RR properties.

The monoclinic metal T' phase of WTe₂, a semimetal with no band gap (Fig. 2b), was synthesized decades ago (Fig. 2a),³² a characteristic corroborated by the calculated partial density of states (PDOS) in Fig. S6 (ESI†). T'-WTe₂ features three atomic layers, with nonequivalent top (Te₁ and Te₂) and bottom (Te₃ and Te₄) Te layers. The Te₁ atom sits higher than Te₂ in

the top layer, forming what we term as a ‘nonuniform surface’,³³ with bond lengths of 2.72 Å ($L_{\text{Te}_2-\text{W}}$) and 2.83 Å ($L_{\text{Te}_1-\text{W}}$).

3.3. CO₂ adsorption and electroreduction for Cu_n@T'-WTe₂ ($n = 3, 8, 13$)

Firstly, we investigate the adsorption of Cu_n ($n = 3, 8, 13$) clusters on the T'-WTe₂ substrate, with all optimized configurations presented in Fig. S3–S5 (ESI†). The most stable structures for Cu₃@T'-WTe₂ (Fig. S3b, ESI†), Cu₈@T'-WTe₂ (Fig. S4h, ESI†), and Cu₁₃@T'-WTe₂ (Fig. S5d, ESI†) are highlighted in Fig. 3 for further studying the CO₂RR. Bader charge analysis (Table S1, ESI†) reveals electron transfers of 0.28e, 0.32e and 0.18e from Cu₃, Cu₈, and Cu₁₃ to T'-WTe₂, respectively, indicating significant substrate–cluster interactions, further evidenced by orbital hybridization in the PDOS (Fig. S7, ESI†). As noted in Section 2, while isolated Cu_n clusters exhibit size-dependent magnetism, the interaction with the T'-WTe₂ substrate leads to complete spin quenching. The AIMD simulation at 500 K over 5ps (Fig. S11, ESI†) shows no structural degradation, confirming the excellent thermal stability of the Cu_n@T'-WTe₂ catalyst under ambient conditions.

To assess the substrate's role in the CO₂RR performance, we studied CO₂ adsorption on the Cu₃@T'-WTe₂, Cu₈@T'-WTe₂, and Cu₁₃@T'-WTe₂ surfaces. Various adsorption configurations of CO₂ on the catalyst surfaces are considered as shown in Fig. S8 (ESI†). Strong adsorption energy typically elongates the C–O bond length in the adsorbed CO₂ molecule.^{17,54,55} Fig. 3 presents the most favorable sites for CO₂ adsorption, showing $L_{\text{C}-\text{O}}$ extended to 1.22 Å and 1.88 Å (Fig. 3a), 1.25 Å and 1.28 Å (Fig. 3d), and 1.26 Å (Fig. 3g) for the Cu₃@T'-WTe₂,

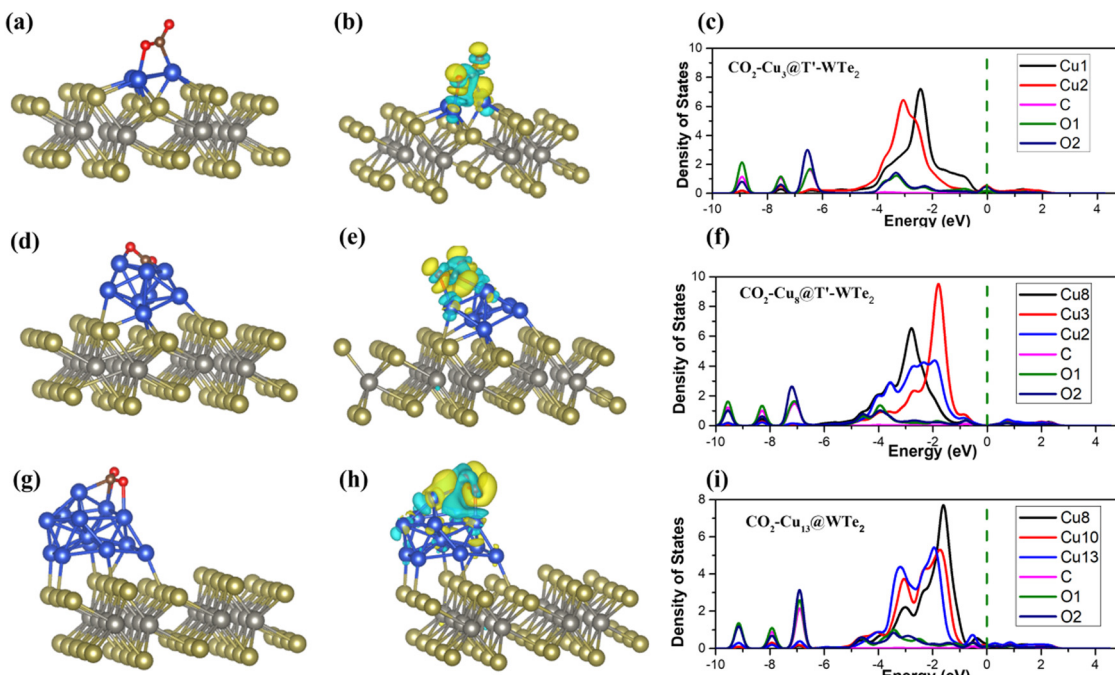


Fig. 3 The most stable adsorption configurations, the isosurface of the charge density difference with an isovalue of 0.003 \AA^{-3} , and the PDOS for CO₂ on Cu₃@WTe₂: (a)–(c), Cu₈@WTe₂ (d)–(f) and Cu₁₃@WTe₂ (g)–(i). The blue (yellow) wireframes denote the loss (gain) of electrons with the isosurface values set as 0.003 \AA^{-3} . The Fermi level is assigned at 0 eV.

Table 2 Parameters of adsorbed CO₂ on the Cu_n@WTe₂ ($n = 3, 8, 13$). Including adsorption free energies ($E_{\text{ads-free}}$), O=C=O angles ($\angle \text{OCO}$), the corresponding C=O bond lengths ($L_{\text{C=O}}$) of Cu_n@WTe₂ ($n = 3, 8, 13$), and the net charge transferred from adsorbents to CO₂ (Ag is calculated based on the Bader charges)

Adsorption configurations	$E_{\text{ads-free}}$ (eV)	$\angle \text{OCO}$	$L_{\text{C-O}}$ (Å)	Δq (e)
$\text{CO}_2\text{-Cu}_3@\text{WTe}_2$	-0.10	134.2°	1.22; 1.28	0.62
$\text{CO}_2\text{-Cu}_8@\text{WTe}_2$	-0.33	130.6°	1.25; 1.28	0.79
$\text{CO}_2\text{-Cu}_{13}@\text{WTe}_2$	0.02	132.3°	1.26	0.74

$\text{Cu}_8@\text{T}'\text{-WTe}_2$ and $\text{Cu}_{13}@\text{T}'\text{-WTe}_2$ systems, respectively, suggesting enhanced activation of CO_2 . After CO_2 adsorption, the linear $\text{O}=\text{C}=\text{O}$ geometry bends into a V-shape, with the ($\angle \text{OCO}$ angles decreasing from 179.9° to 134.2° for $\text{Cu}_3@\text{WTe}_2$) (Table 2). Similarly, the same trend can be observed for $\text{Cu}_8@\text{WTe}_2$ and $\text{Cu}_{13}@\text{WTe}_2$, indicating effective CO_2 activation by $\text{Cu}_n@\text{WTe}_2$. The PDOS analysis shown in Fig. 3c, f, and i

reveals orbital hybridization and charge transfer between Cu, C, and O atoms, underscoring the strong interaction between the CO₂ molecules and the Cu_n@T'-WTe₂ catalysts.^{11,56,57} The charge density difference (see Fig. 3) and the Bader charge analysis (Table 2) further confirm electron donation from Cu_n@WTe₂ to the CO₂ molecule (around 0.62e–0.79e). The broadly dispersed PDOS peaks for C and O relative to isolated CO₂ molecules (Fig. S9, ESI†) and the hybridization with Cu atoms also support the strong interaction between CO₂ and Cu_n.

3.4. CO₂ reduction reaction pathways on the Cu_n@WTe₂ ($n = 3, 8, 13$)

We next explore the CO₂RR pathways on Cu_n@WTe₂. Fig. 4 illustrates the calculated free energy profile for the most favorable CO₂RR pathways on Cu₃@WTe₂, Cu₈@WTe₂, and Cu₁₃@WTe₂, with the corresponding optimal reaction configurations shown in Fig. S10 (ESI[†]). For CO₂-Cu₃@WTe₂, the

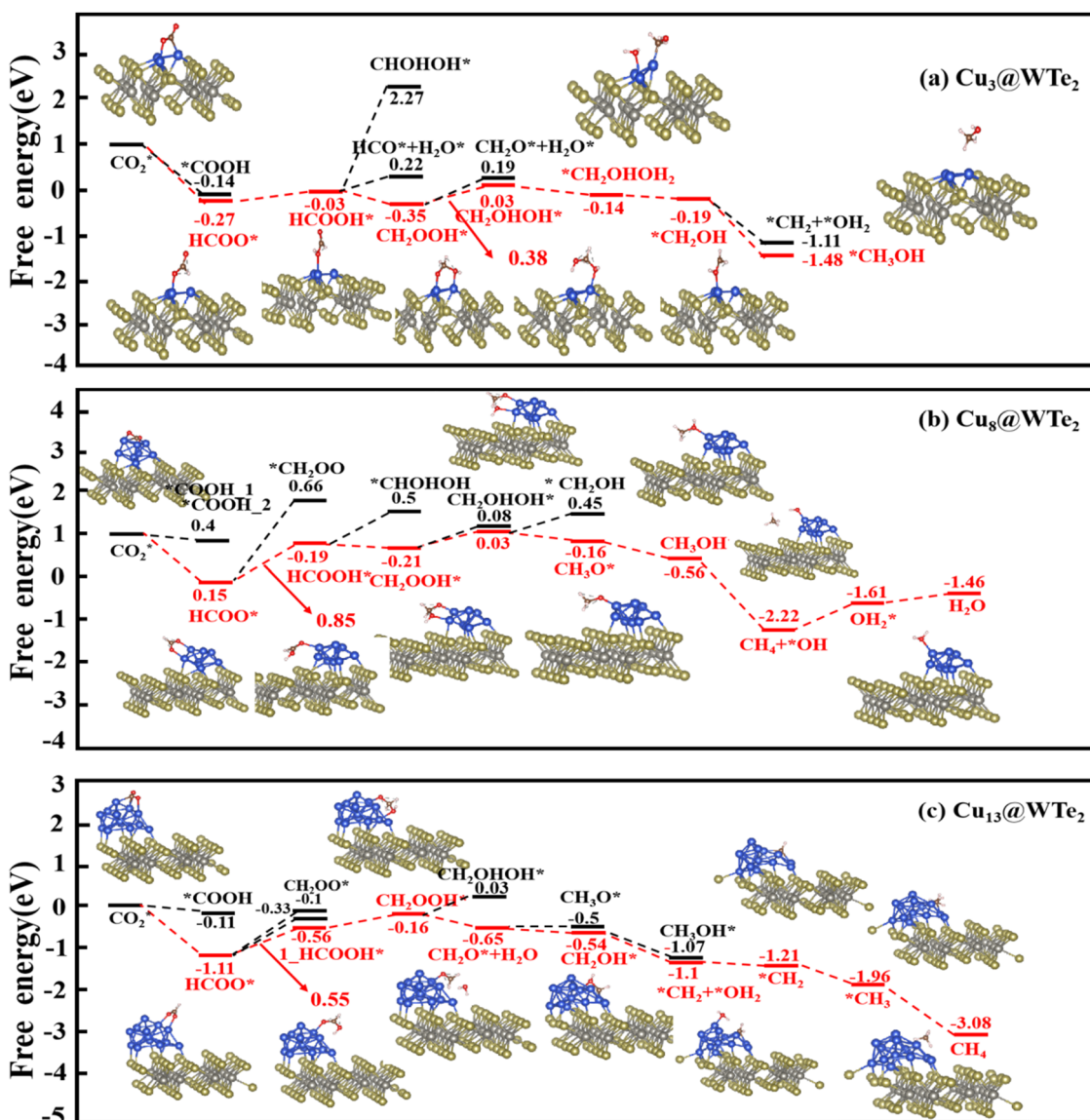


Fig. 4 Free energy diagram for the electrochemical CO₂RR on (a) Cu₃@WTe₂, (b) Cu₈@WTe₂, and (c) Cu₁₃@WTe₂.

Table 3 The calculated U_L ($|U_L|$), HCOO intermediate adsorption (ΔG_{HCOO^*}) and final product of CO₂RR, and the H* intermediate adsorption (ΔG_{H^*}) of the HER with Cu_n@WTe₂ ($n = 3, 8, 13$) catalysts

Configurations	CO ₂ RR		HER		
	$ U_L $ (V)	ΔG_{HCOO^*} (eV)	Product	$ U_L $ (V)	ΔG_{H^*} (eV)
Cu ₃ @WTe ₂	0.38	-0.27	CH ₃ OH	0.10	0.10
Cu ₈ @WTe ₂	0.86	-1.04	CH ₄	0.05	-0.05
Cu ₁₃ @WTe ₂	0.55	-1.11	CH ₄	0.85	-0.85

initial H⁺ and e⁻ pair attacks the carbon atom of CO₂, forming HCOO* with a free energy change of -0.27 eV. Subsequent hydrogenation yields HCOOH*, followed by an exothermic step forming CH₂OOH* as shown in Fig. 4a, which is energetically more preferred than the formation of CHOHOH* or HCO* + H₂O*. Further hydrogenation of CH₂OOH* favors CH₂OHOH* ($\Delta G < 0$) over CH₂O* + H₂O*. Two subsequent additions of the H⁺ and e⁻ pair will attack the O atom, releasing the H₂O molecule and leaving *CH₂OH, which undergoes successive hydrogenation steps to produce CH₃OH molecules. Overall, the PDS is the formation of CH₂OHOH* from CH₂OOH* with a U_L of -0.38 V.

For the Cu₈@WTe₂ and Cu₁₃@WTe₂ surface, the initial step of the CO₂RR is the formation of HCOO*, followed by hydrogenation of HCOO* to form HCOOH* (see Fig. 4b and c), which is more energetically favorable than that of CH₂OO*. HCOOH* then converts to CH₂OOH*. On Cu₈@WTe₂, CH₂OOH* after hydrogenation will transform into CH₂O* + *OH₂, proceeding to CH₃OH* and ultimately producing CH₄. On Cu₁₃@WTe₂, CH₂OOH will be further hydrogenated to CH₂O* with H₂O release, followed by hydrogenation to *CH₄ with the final release of the CH₄ molecule. The PDS for both the Cu₈@WTe₂ and Cu₁₃@WTe₂ systems is HCOO* → HCOOH*, with U_L values of -0.85 V and -0.55 V, respectively. The free energy values (G(T)) for these pathways are detailed in Table S3 (ESI†).

The analysis reveals that Cu₃@WTe₂, Cu₈@WTe₂, and Cu₁₃@WTe₂ all exhibit robust CO₂RR activity. On Cu₃@WTe₂, CO₂RR proceeds via a 6e⁻ charge transfer pathway, yielding CH₃OH, whereas Cu₈@WTe₂ and Cu₁₃@WTe₂ favor an 8e⁻ charge transfer reaction pathway, producing CH₄ as the primary product. Comparison of the overpotentials with pure Cu_n clusters (Table S2, ESI†) shows that Cu_n on the T'-WTe₂ substrate outperforms their standalone counterparts, with lower $|U_L|$ values indicating enhanced CO₂RR efficiency. Specifically, $|U_L|$ for Cu₃@WTe₂ is 0.38 V (vs. 0.64 V for pure Cu₃, a 0.26 V reduction), while $|U_L|$ for Cu₁₃@WTe₂ is 0.55 V (vs. 0.89 V for pure Cu₁₃, a 0.34 V reduction). This suggests that the T'-WTe₂ substrate significantly boosts the CO₂RR performance, with the enhancement scaling with Cu cluster size.

3.5. Analysis of the hydrogen evolution reaction and solvent effects

To evaluate the competing HER,¹⁸ we analyzed the HER performance on Cu_n@WTe₂ ($n = 3, 8, 13$), as detailed in Fig S12 and S14 (ESI†). In all the optimized configurations, H atoms preferentially bind to Cu clusters rather than the WTe₂ surface.

Catalytic selectivity was assessed using the difference in U_L values, *i.e.*, $|U_{\text{L}(\text{CO}_2)}| - |U_{\text{L}(\text{H}_2)}|$,³⁷ where a positive value of $|U_{\text{L}(\text{CO}_2)}| - |U_{\text{L}(\text{H}_2)}|$ indicates a poor CO₂RR selectivity over the HER. For the Cu₁₃@T'-WTe₂, the $|U_{\text{L}(\text{CO}_2)}| - |U_{\text{L}(\text{H}_2)}|$ is calculated to be -0.30 V (see Table 3), suggesting a better CO₂RR selectivity over the HER. Given that HCOO* is a critical intermediate in all CO₂RR pathways, we then considered the competition between H* and HCOO*.^{55,58-60} For the Cu₁₃@WTe₂, HCOO* formation (Fig. 4c) has a free energy change of -1.11 eV, more favorable than -0.85 eV for the HER process (see Table 3), indicating greater HCOO* stability over H*.

To further gain an in-depth understanding of the catalyst effects, we compared the DOS curves of isolated and adsorbed HCOO* intermediates on the catalyst. As shown in Fig S15 (ESI†), the 2p orbitals of O and C atoms after adsorption shift toward lower energy region near the Fermi level, with larger shifts reflecting stronger intermediate–substrate interaction, and the lower adsorption energy.^{17,61,62} Cu₁₃@WTe₂ exhibits the lowest adsorption energy (-1.11 eV) compared to -0.27 eV for Cu₃@WTe₂. This suggests that the buckled T'-WTe₂ surface enhances CO₂RR activity in the supported Cu_n nanocluster, with larger cluster size strengthening substrate–Cu interactions and boosting electrocatalytic CO₂ reduction.

Overall, Cu₁₃@WTe₂ emerges as the optimal CO₂RR electrocatalyst among the studied configurations. We further examine its electrochemical CO₂RR performance using free energy diagrams with an implicit solvation model (Fig. S16, ESI†). The PDS remains unchanged, with the U_L value shifting by only 0.09 V upon incorporating the solvation effect. These findings suggest that the electrolyte environment exerts minimal influence on the CO₂RR performance of the Cu₁₃@WTe₂ catalysts.

4. Conclusions

In conclusion, we theoretically investigate the CO₂ electrocatalytic properties on pure Cu clusters and their performance when supported on a T'-WTe₂ substrate. Our results reveal that the introduction of the WTe₂ substrate significantly reduces the CO₂RR overpotential across the system, with Cu₁₃@WTe₂ exhibiting particularly notable suppression of the competing hydrogen evolution reaction (HER). Our findings elucidate the size-dependent electrocatalytic behavior of the CO₂RR and HER across different Cu clusters while highlighting the critical role of the substrate in modulating electrochemical performance. Collectively, this work offers valuable insights and a strategic framework for designing efficient CO₂RR catalysts, paving the way for future experimental advancement in electrocatalytic systems.

Author contributions

Qian Sun: data curation, writing – original draft. Huiru Yang: revise the manuscript. Chunmei Zhang: writing – original draft, writing – review & editing. Aijun Du: revise the manuscript and

technical support. All authors contributed to the results interpretation and manuscript preparation.

Data availability

The data presented in this work is available from the corresponding author upon reasonable request.

Conflicts of interest

There is no conflict to declare.

References

- Y. Shi, M. Chen and F. Wang, In Research on energy-saving of the pebble thermoregulation greenhouse, Global Conference on Civil, Structural and Environmental Engineering/3rd International Symp on Multi-field Coupling Theory of Rock and Soil Media and its Applications, China Three Gorges Univ, Yichang, PEOPLES R CHINA, 2012, Oct 20–21, China Three Gorges Univ, Yichang, PEOPLES R CHINA, 2012, pp. 2112–2115.
- Y. Shi and M. Chen, In Study on temperature distribution regularity of pebble thermoregulation greenhouse, Global Conference on Civil, Structural and Environmental Engineering/3rd International Symp on Multi-field Coupling Theory of Rock and Soil Media and its Applications, China Three Gorges Univ, Yichang, PEOPLES R CHINA, 2012 Oct 20–21, China Three Gorges Univ, Yichang, PEOPLES R CHINA, 2012, pp. 2116–2119.
- D. J. D. Pimlott, A. Jewlal, Y. Kim and C. P. Berlinguette, Oxygen-Resistant CO₂ Reduction Enabled by Electrolysis of Liquid Feedstocks, *J. Am. Chem. Soc.*, 2023, **145**(48), 25933–25937.
- Y. Zhang, In On Study of Teaching Reform of Organic Chemistry Course in Applied Chemical Industry Technology, 2017 3rd International Conference on Energy, Environment and Materials Science (EEMS), Northwestern Polytechnical University, Singapore, SINGAPORE, 2017 Jul 28–30, Northwestern Polytechnical University, Singapore, SINGAPORE, 2017.
- G. Liu, X. Mao, B. Yang, J. Shang and Z. Wu, Research progress on chemical looping reforming of macromolecular components of volatiles from biomass pyrolysis based on decoupling strategy, *Fuel Process. Technol.*, 2022, **235**, 107375.
- S. Fu, I. Angelidaki and Y. Zhang, In situ Biogas Upgrading by CO₂-to-CH₄ Bioconversion, *Trends Biotechnol.*, 2021, **39**(4), 336–347.
- M. Shen, L. Zhang and J. Shi, Defect Engineering of Photocatalysts towards Elevated CO₂ Reduction Performance, *ChemSusChem*, 2021, **14**(15), 3226.
- X. Feng, Y. Pi, Y. Song, C. Brzezinski, Z. Xu, Z. Li and W. Lin, Metal-Organic Frameworks Significantly Enhance Photocatalytic Hydrogen Evolution and CO₂ Reduction with Earth-Abundant Copper Photosensitizers, *J. Am. Chem. Soc.*, 2020, **142**(2), 690–695.
- A. R. Woldu, Z. Huang, P. Zhao, L. Hu and D. Astruc, Electrochemical CO₂ reduction (CO₂RR) to multi-carbon products over copper-based catalysts, *Coord. Chem. Rev.*, 2022, **454**, 214340.
- Z.-Y. Du, K. Wang, S.-B. Li, Y.-M. Xie, J.-H. Tian, Q.-N. Zheng, W. F. Ip, H. Zhang, J.-F. Li and Z.-Q. Tian, In Situ Raman Spectroscopic Studies of Electrochemical CO₂ Reduction on Cu-Based Electrodes, *J. Phys. Chem. C*, 2024, **128**(28), 11741–11755.
- Z. Zhao, Z. Chen, X. Zhang and G. Lu, Generalized Surface Coordination Number as an Activity Descriptor for CO₂ Reduction on Cu Surfaces, *J. Phys. Chem. C*, 2016, **120**(49), 28125–28130.
- T. Liu, G. Song, X. Liu, Z. Chen, Y. Shen, Q. Wang, Z. Peng and G. Wang, Insights into the mechanism in electrochemical CO₂ reduction over single-atom copper alloy catalysts: A DFT study, *Iscience*, 2023, **26**(10), 107953.
- H. Dong, Y. Li and D.-E. Jiang, First-Principles Insight into Electrocatalytic Reduction of CO₂ to CH₄ on a Copper Nanoparticle, *J. Phys. Chem. C*, 2018, **122**(21), 11392–11398.
- M. Rozenberg, A. Loewenschuss and C. J. Nielsen, H-Bonding of Formic Acid with Its Decomposition Products: A Matrix Isolation and Computational Study of the HCOOH/CO and HCOOH/CO₂ Complexes, *J. Phys. Chem. A*, 2015, **119**(31), 8497–8502.
- S. Xue, X. Liang, Q. Zhang, X. Ren, L. Gao, T. Ma, A. Liu and I. A. Pasti, Density Functional Theory Study of CuAg Bimetal Electrocatalyst for CO₂RR to Produce CH₃OH, *Catalysts*, 2024, **14**(1), 7.
- C. Christophe, Silica-supported PdGa Nanoparticles: Metal Synergy for Highly Active and Selective CO₂-to-CH₃OH Hydrogenation, *JACS Au*, 2022, **2**(8), 1946–1947.
- P. Saha, S. Amanullah and A. Dey, Selectivity in Electrochemical CO₂ Reduction, *Acc. Chem. Res.*, 2022, **55**(2), 134–144.
- C. Kim, J. Kim, S. Joo, Y. Yang, J. Shin, M. Liu, J. Cho and G. Kim, Highly Efficient CO₂ Utilization via Aqueous Zinc- or Aluminum- CO₂ Systems for Hydrogen Gas Evolution and Electricity Production, *Angew. Chem., Int. Ed.*, 2019, **58**(28), 9506–9511.
- J. Gao, H. Wang, K. Feng, C. Xiang, H. Wang, H. Qi, Y. Liu, H. Tian, J. Zhong and Z. Kang, Cu atomic clusters on N-doped porous carbon with tunable oxidation state for the highly-selective electroreduction of CO₂, *Mater. Adv.*, 2020, **1**(7), 2286–2292.
- H. Xie, T. Wang, J. Liang, Q. Li and S. Sun, Cu-based nanocatalysts for electrochemical reduction of CO₂, *Nano Today*, 2018, **21**, 41–54.
- Y. Xia, Q. Zhang, F. Guo, J. Wang, W. Li and J. Xu, Ag@Cu with Cu-CuO interface prepared by air cold-plasma promoting the electrocatalytic reduction of CO₂ to low-carbon alcohols, *Vacuum*, 2022, **196**, 110767.
- S. Choe, J. Kim, S. Y. Kim and S. H. Ahn, Controlling the surface oxidation state of halogenated Cu-based catalyst for electrochemical reduction of carbon dioxide to ethylene, *J. Alloys Compd.*, 2024, 1005.

23 X.-X. Li, L. Zhang, J. Liu, L. Yuan, T. Wang, J.-Y. Wang, L.-Z. Dong, K. Huang and Y.-Q. Lan, Design of Crystalline Reduction-Oxidation Cluster-Based Catalysts for Artificial Photosynthesis, *JACS Au*, 2021, **1**(8), 1288–1295.

24 Y. Gao, M. Zhao, L. Jiang and Q. Yu, Electrochemical CO₂ reduction of graphene single-atom/cluster catalysts, *Mol. Catal.*, 2024, **562**, 114225.

25 S.-Y. Wu, T.-C. Chuang and H.-T. Chen, Electrochemical CO₂ reduction on Single-Atom aluminum catalysts supported on graphene and N-doped Graphene: Mechanistic insights and hydration effects, *Appl. Surf. Sci.*, 2025, **681**, 161523.

26 E. Plaza-Mayoral, V. Okatenko, K. N. Dalby, H. Falsig, I. Chorkendorff, P. Sebastian-Pascual and M. Escudero-Escribano, Composition effects of electrodeposited Cu-Ag nanostructured electrocatalysts for CO₂ 2 reduction, *Iscience*, 2024, **27**(6), 109933.

27 X.-G. Zhang, S. Feng, C. Zhan, D.-Y. Wu, Y. Zhao and Z.-Q. Tian, Electrocatalysis Reaction Mechanism of Carbon Dioxide to C₂ Products via Cu/Au Bimetallic Catalysis: A Theoretical Prediction, *J. Phys. Chem. Lett.*, 2020, **11**(16), 6593–6599.

28 D. Gao, S. Rao, Y. Li, N. Liu and D. Wang, Enhancement of CO adsorption energy on defective graphene-supported Cu₁₃ cluster and prediction with an induction energy model, *Appl. Surf. Sci.*, 2023, **615**, 156368.

29 A. Y. Ermilov, A. V. Soloviev, Y. N. Morosov and T. I. Shabatina, Interaction of Copper Clusters with Dioxidine, *Moscow Univ. Chem. Bull.*, 2024, **79**(4), 233–238.

30 H. Yang, W. Zou, C. Zhang and A. Du, Ab Initio Studies of Electrocatalytic CO₂ Reduction for Small Cu Cluster Supported on Polar Substrates, *ACS Appl. Mater. Interfaces*, 2024, **16**(26), 33688–33695.

31 C. Huang, A. Narayan, E. Zhang, Y. Liu, X. Yan, J. Wang, C. Zhang, W. Wang, T. Zhou, C. Yi, S. Liu, J. Ling, H. Zhang, R. Liu, R. Sankar, F. Chou, Y. Wang, Y. Shi, K. T. Law, S. Sanvito, P. Zhou, Z. Han and F. Xiu, Inducing Strong Superconductivity in WTe₂ by a Proximity Effect, *ACS Nano*, 2018, **12**(7), 7185–7196.

32 P. Zhang, P. Li, Q. Ma, M. Shen, Z. Tian and Y. Liu, Interfacial properties of In-plane monolayer 2H-MoTe₂/1T'-WTe₂ heterostructures, *Appl. Surf. Sci.*, 2023, **623**, 157022.

33 Y. Maximenko, Y. Chang, G. Chen, M. R. Hirsbrunner, W. Swiech, T. L. Hughes, L. K. Wagner and V. Madhavan, Nanoscale studies of electric field effects on monolayer 1T'-WTe₂, *Npj Quant. Mater.*, 2022, **7**(1), 29.

34 V. E. Matulis, O. A. Ivashkevich and V. S. Gurin, DFT study of electronic structure and geometry of anionic copper clusters, *J. Mol. Struct. Theochem.*, 2004, **681**(1–3), 169–176.

35 Q. Zeng, X. Wang, M. L. Yang and H. B. Fu, Interplay between geometrical and electronic stability of neutral and anionic Cu₁₃ clusters: a first-principles study, *Eur. Phys. J.*, 2010, **58**(1), 125–129.

36 C. A. Barboza, A. Gambetta, R. Arratia-Perez, P. L. Rodriguez-Kessler, A. Munoz-Castro and D. MacLeod-Carey, Structural, electronic and magnetic properties of copper(I) cubic clusters, *Polyhedron*, 2021, **195**, 114878.

37 G. Henkelman, B. P. Uberuaga and H. Jónsson, A climbing image nudged elastic band method for finding saddle points and minimum energy paths, *J. Chem. Phys.*, 2000, **113**(22), 9901–9904.

38 K. Furthmuller, Efficient iterative schemes for ab initio total-energy calculations using a plane-wave basis set, *Phys. Rev. B: Condens. Matter Mater. Phys.*, 1996, **54**(16), 11169–11186.

39 J. Hafner, Ab-initio simulations of materials using VASP:: Density-functional theory and beyond, *J. Comput. Chem.*, 2008, **29**(13), 2044–2078.

40 K. Burke, J. P. Perdew and M. Levy, Improving energies by using exact electron densities, *Phys. Rev. A: At., Mol., Opt. Phys.*, 1996, **53**(5), R2915–R2917.

41 X. Xu and W. A. Goddard, The extended Perdew-Burke-Ernzerhof functional with improved accuracy for thermodynamic and electronic properties of molecular systems, *J. Chem. Phys.*, 2004, **121**(9), 4068–4082.

42 P. E. Blöchl, Projector augmented-wave method, *Phys. Rev. B: Condens. Matter Mater. Phys.*, 1994, **50**(24), 17953–17979.

43 S. Grimme, J. Antony, S. Ehrlich and H. Krieg, A consistent and accurate ab initio parametrization of density functional dispersion correction (DFT-D) for the 94 elements H-Pu, *J. Chem. Phys.*, 2010, **132**(15), 154104.

44 H. S. Lee and M. E. Tuckerman, Ab initio molecular dynamics with discrete variable representation basis sets: Techniques and application to liquid water, *J. Phys. Chem. A*, 2006, **110**(16), 5549–5560.

45 G. Fisicaro, L. Genovese, O. Andreussi, N. Marzari and S. Goedecker, A generalized Poisson and Poisson-Boltzmann solver for electrostatic environments, *J. Chem. Phys.*, 2016, **144**(1), 014103.

46 A. Lahanas and V. Tsoussidis, Exploiting the efficiency and fairness potential of AIMD-based congestion avoidance and control, *Comput. Networks*, 2003, **43**(2), 227–245.

47 J. K. Nørskov, J. Rossmeisl, A. Logadottir, L. Lindqvist, J. R. Kitchin, T. Bligaard and H. Jónsson, Origin of the Overpotential for Oxygen Reduction at a Fuel-Cell Cathode, *J. Phys. Chem. B*, 2004, **108**(46), 17886–17892.

48 V. Wang, N. Xu, J.-C. Liu, G. Tang and W.-T. Geng, VASPKIT: A user-friendly interface facilitating high-throughput computing and analysis using VASP code, *Comput. Phys. Commun.*, 2021, **267**, 108033.

49 G. Guzman-Ramirez, F. Aguilera-Granja and J. Robles, DFT study of the fragmentation channels and electronic properties of Cu_n^ν (ν = ±1,0,2; n = 3–13) clusters, *Eur. Phys. J. D*, 2010, **57**(3), 335–342.

50 V. L. Mazalova, A. V. Soldatov, S. Adam, A. Yakovlev, T. Moeller and R. L. Johnston, Small Copper Clusters in Ar Shells: A Study of Local Structure, *J. Phys. Chem. C*, 2009, **113**(21), 9086–9091.

51 V. E. Matulis, D. M. Palagin, A. S. Mazheika and O. A. Ivashkevich, DFT study of electronic structure and geometry of anionic copper clusters Cu_n[−] (n = 11, 12, 13), *J. Mol. Struct. Theochem.*, 2008, **857**(1–3), 66–71.

52 E. E. Karagiannis, C. E. Kefalidis, I. Petrakopoulou and C. A. Tsipis, Density Functional Study of Structural,

Electronic, and Optical Properties of Small Bimetallic Ruthenium-Copper Clusters, *J. Comput. Chem.*, 2011, **32**(7), 1241–1261.

53 H. Yang, W. Zou, K. Ostrikov, C. Zhang and A. Du, Tuning electrocatalytic nitrogen reduction on supported nickel cluster via substrate phase engineering, *Appl. Surf. Sci.*, 2023, **640**, 158277.

54 Y. Gao, X. Tu, X. Liu, Y. Zhang, M. Huang, J. Zhu and H. Jiang, Advances in DFT study of electronic structure and geometry of anionic copper clusters CO_2 Electroreduction over Hollow Fiber Gas Diffusion Electrodes, *ChemCatChem*, 2024, **16**, 17.

55 M. Hu, L. Li, J. Li, K. Zahra and Z. Zhang, Two-dimensional Cu-based materials for electrocatalytic carbon dioxide reduction, *Iscience*, 2024, **27**(3), 109313.

56 W. Choi, Y. Chae, E. Liu, D. Kim, W. S. Drisdell, H.-S. Oh, J. H. Koh, D. K. Lee, U. Lee and D. H. Won, Exploring the influence of cell configurations on Cu catalyst reconstruction during CO_2 electroreduction, *Nat. Commun.*, 2024, **15**(1), 8345.

57 W. Nie, G. P. Heim, N. B. Watkins, T. Agapie and J. C. Peters, Organic Additive-derived Films on Cu Electrodes Promote Electrochemical CO_2 Reduction to C_2^+ Products Under Strongly Acidic Conditions, *Angew. Chem., Int. Ed.*, 2023, **62**(12), 202216102.

58 C. Christophe, Silica-supported PdGa Nanoparticles: Metal Synergy for Highly Active and Selective CO_2 -to- CH_3OH Hydrogenation, *JACS Au*, 2021, **2**(8), 1946–1947.

59 Q. Xu, J. Jiang, X. Sheng, Q. Jing, X. Wang, L. Duan and H. Guo, Understanding the synergistic effect of piezoelectric polarization and the extra electrons contributed by oxygen vacancies on an efficient piezo-photocatalysis CO_2 reduction, *Inorg. Chem. Front.*, 2023, **10**(10), 2939–2950.

60 R. Cai, M. Sun, J. Ren, M. Ju, X. Long, B. Huang and S. Yang, Unexpected high selectivity for acetate formation from CO_2 reduction with copper based 2D hybrid catalysts at ultralow potentials, *Chem. Sci.*, 2021, **12**(46), 15382–15388.

61 O. F. Lopes and H. Varela, Effect of Annealing Treatment on Electrocatalytic Properties of Copper Electrodes toward Enhanced CO_2 Reduction, *ChemistrySelect*, 2018, **3**(31), 9046–9055.

62 Q. Chang, J. H. Lee, Y. Liu, Z. Xie, S. Hwang, N. S. Marinkovic, A.-H. A. Park, S. Kattel and J. G. Chen, Electrochemical CO_2 Reduction Reaction over Cu Nanoparticles with Tunable Activity and Selectivity Mediated by Functional Groups in Polymeric Binder, *Jacs Au*, 2022, **2**(1), 214–222.